Nanoscale topography and spatial light modulator characterization using wide-field quantitative phase imaging

Gannavarpu Rajshekhar,[1] Basanta Bhaduri,[1] Chris Edwards,[2] Renjie Zhou,[2] Lynford L. Goddard,[2] and Gabriel Popescu[1,*]

[1] *Quantitative Light Imaging Laboratory, Department of Electrical and Computer Engineering, Beckman Institute for Advanced Science and Technology, University of Illinois at Urbana-Champaign, Urbana-61801, Illinois, USA*

[2] *Photonic Systems Laboratory, Department of Electrical and Computer Engineering, Micro and Nanotechnology Laboratory, University of Illinois at Urbana-Champaign, Urbana-61801, Illinois, USA*

[*] *gpopescu@illinois.edu*

Abstract: We demonstrate an optical technique for large field of view quantitative phase imaging of reflective samples. It relies on a common-path interferometric design, which ensures high stability without the need for active stabilization. The technique provides single-shot, full-field and robust measurement of nanoscale topography of large samples. Further, the inherent stability allows reliable measurement of the temporally varying phase retardation of the liquid crystal cells, and thus enables real-time characterization of spatial light modulators. The technique's application potential is validated through experimental results.

© 2014 Optical Society of America

OCIS codes: (110.3175) Interferometric imaging; (120.3930) Metrological instrumentation; (070.6120) Spatial light modulators; (120.5050) Phase measurement.

References and links

1. D. J. Whitehouse, "Surface metrology," Meas. Sci. Technol. **8**, 955–972 (1997).
2. J. M. Bennett and J. H. Dancy, "Stylus profiling instrument for measuring statistical properties of smooth optical surfaces," Appl. Opt. **20**, 1785–1802 (1981).
3. J. H. Jang, W. Zhao, J. W. Bae, D. Selvanathan, S. L. Rommel, I. Adesida, A. Lepore, M. Kwakernaak, and J. H. Abeles, "Direct measurement of nanoscale sidewall roughness of optical waveguides using an atomic force microscope," Appl. Phys. Lett. **83**, 4116–4118 (2003).
4. J. E. Castle and P. A. Zhdan, "Characterization of surface topography by SEM and SFM: Problems and solutions," J. Phys. D: Appl. Phys. **30**, 722–740 (1997).
5. L. Deck and P. de Groot, "High-speed noncontact profiler based on scanning white-light interferometry," Appl. Opt. **33**, 7334–7338 (1994).
6. J. C. Wyant, "Computerized interferometric surface measurements," Appl. Opt. **52**, 1–8 (2013).
7. P. Ferraro, C. D. Core, L. Miccio, S. Grilli, S. D. Nicola, A. Finizio, and G. Coppola, "Phase map retrieval in digital holography: avoiding the undersampling effect by a lateral shear approach," Opt. Lett. **32**, 2233–2235 (2007).
8. L. L. Deck, "Environmentally friendly interferometry," Proc. SPIE **5532**, 159–169 (2004).
9. D. M. Sykora and P. de Groot, "Instantaneous interferometry: Another view," International Optical Design Conference and Optical Fabrication and testing, OMA1 (2010).
10. D. M. Sykora and M. L. Holmes, "Dynamic measurements using a Fizeau interferometer," Proc. SPIE **8082**, 80821R (2011).
11. X. Xun and R. W. Cohn, "Phase calibration of spatially nonuniform spatial light modulators," Appl. Opt. **43**, 6400–6406 (2004).

12. H. Zhang, J. Zhang, and L. Wu, "Evaluation of phase-only liquid crystal spatial light modulator for phase modulation performance using a Twyman-Green interferometer," Meas. Sci. Technol. **18**, 1724–1728 (2007).
13. R. Wang, D. Li, M. Hu, and J. Tian, "Phase calibration of spatial light modulators by heterodyne interferometry," Proc. SPIE **7848**, 78481F (2010).
14. L. Hu, L. Xuan, Y. Liu, Z. Cao, D. Li, and Q. Mu, "Phase-only liquid crystal spatial light modulator for wavefront correction with high precision," Opt. Express **12**, 6403–6409 (2004).
15. E. Schonbrun, R. Piestun, P. Jordan, J. Cooper, K. Wulff, J. Courtial, and M. Padgett, "3D interferometric optical tweezers using a single spatial light modulator," Opt. Express **13**, 3777–3786 (2005).
16. M. R. Beversluis, L. Novotny, and S. J. Stranick, "Programmable vector point-spread function engineering," Opt. Express **14**, 2650–2656 (2006).
17. D. J. Cho, S. T. Thurman, J. T. Donner, and G. M. Morris, "Characteristics of a 128 × 128 liquid-crystal spatial light modulator for wave-front generation," Opt. Lett. **23**, 969–971 (1998).
18. J. Oton, P. Ambs, M. S. Millan, and E. Perez-Cabre, "Dynamic calibration for improving the speed of a parallel-aligned liquid-crystal-on-silicon display," Appl. Opt. **48**, 4616–4624 (2009).
19. G. Popescu, T. Ikeda, R. R. Dasari, and M. S. Feld, "Diffraction phase microscopy for quantifying cell structure and dynamics," Opt. Lett. **31**, 775–777 (2006).
20. C. Edwards, A. Arbabi, G. Popescu, and L. L. Goddard, "Optically monitoring and controlling nanoscale topography during semiconductor etching," Light: Science & Applications **1**, e30 (2012).
21. R. Zhou, C. Edwards, A. Arbabi, G. Popescu, and L. L. Goddard, "Detecting 20 nm wide defects in large area nanopatterns using optical interferometric microscopy," Nano Lett. **13**, 3716–3721 (2013).
22. B. Bhaduri, C. Edwards, R. Zhou, H. Pham, L. L. Godard and G. Popescu, "Diffraction phase microscopy: principles and applications in materials and life sciences," Adv. Opt. Photon. (accepted)
23. T. Ikeda, G. Popescu, R. R. Dasari, and M. S. Feld, "Hilbert phase microscopy for investigating fast dynamics in transparent systems," Opt. Lett. **30**, 1165–1167 (2005).
24. D. C. Ghiglia and M. D. Pritt, *Two-Dimensional Phase Unwrapping: Theory, Algorithms, and Software* (Wiley-Interscience, 1998).
25. J. M. Huntley and H. Saldner, "Temporal phase-unwrapping algorithm for automated interferogram analysis," Appl. Opt. **32**, 3047–3052 (1993).

---

1. Introduction

Nanoscale measurement of surface topography is an important problem for material characterization and inspection [1]. Some of the prominent topography measurement techniques include the stylus profilometer [2], atomic force microscope (AFM) [3], scanning electron microscope (SEM) [4], and optical interferometric techniques such as scanning white light interferometer [5], phase-shifting interferometer [6], digital holography method [7] and Fizeau interferometer [8–10]. However, the stylus, AFM and SEM techniques are invasive, and are hence not suitable for non-destructive testing and evaluation. Also, the AFM and SEM techniques have low throughputs, and are not feasible for inspecting large samples. Though the scanning and phase-shifting interferometers are non-invasive, they require multiple scans or phase-shifted frames, and are hence not suitable for dynamic measurements. Also, the interfering beams in phase-shifting interferometer and digital holography travel in separate paths, making them more susceptible to external disturbances and vibrations. Though the Fizeau interferometer has a common-path geometry, it requires the addition of an additional reference surface which influences the fringe contrast, and is prone to multiple reflections.

In addition to surface topography, the optical interferometric techniques have also been applied for refractive index measurements on account of their high sensitivity to optical path length changes; a measurement capability not possible with the stylus, AFM and SEM techniques. In particular, a prominent application has been spatial light modulator (SLM) characterization by phase retardation measurement [11–13]. The SLM is a wavefront modulation device, capable of modulating the polarization, amplitude or phase of the incident light. When a pattern is projected on the SLM, it causes a change in orientation of the birefringent liquid crystal molecules depending on the grayscale values of the pattern, and the reflected light is phase-shifted or retarded with respect to the incident light. By changing the grayscale value of the projected pattern on the SLM, variable phase retardation can be achieved. This has enabled

#201422 - $15.00 USD Received 15 Nov 2013; revised 20 Dec 2013; accepted 14 Jan 2014; published 5 Feb 2014
(C) 2014 OSA

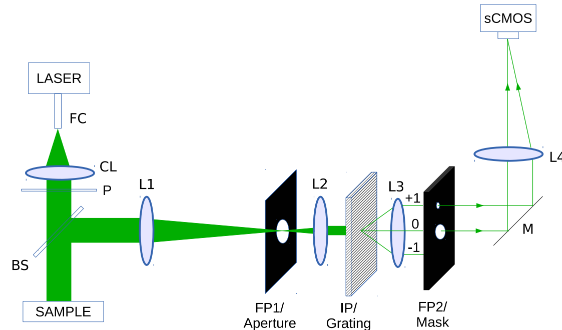

Fig. 1. Wide-field QPI setup. FC: Fiber Coupler, CL:Collimator lens, P:Polarizer, BS:Beam Splitter, L1-L4:Lenses with 400 mm focal length, L2-L3:Lenses with 75 mm focal length, FP1:Fourier Plane of lens L1, IP:Image Plane, FP2:Fourier Plane of lens L3, M:Mirror.

the application of SLM in diverse areas such as adaptive optics [14], optical tweezers [15], microscopy [16] etc. In particular, temporal characterization of the SLM, i.e. reliable estimation of the temporally varying phase retardation is required for several applications [17, 18]. However, it remains a challenging problem due to high temporal stability required for the measurement.

Some of these limitations were addressed by the recently proposed common-path optical technique based on diffraction phase microscopy (DPM) [19–21]. However, the high resolution instruments developed so far based on this approach have been restricted to limited field of view (FOV) imaging, and cannot be applied for inspecting large regions of interest. Here, we propose a wide-field quantitative phase imaging (wQPI) technique that enables the assessment of large area samples with high temporal stability and single-shot full-field measurement capability.

2. Setup

The schematic of the setup is shown in Fig. 1. We use a frequency doubled NdYAG laser, with wavelength $\lambda = 532$ nm, as the light source, whose output is coupled to a single mode fiber and subsequently expanded and collimated using a lens (CL). We also place a polarizer (P) in the optical path to control the polarization and intensity of the illuminating beam. The reflected wave from the sample is guided via the beam splitter (BS) to a $4f$ system comprised of the lenses L1 (focal length $f_1 = 400$ mm) and L2 (focal length $f_2 = 75$ mm), with an aperture (8 mm diameter) in the Fourier plane FP1. At intermediate image plane IP, we obtain the image of the sample with a magnification $M_1 = -f_2/f_1$.

A blazed diffraction grating (300 lines per mm) is placed at the plane IP, which generates multiple diffraction orders, with the positive first order having the highest intensity (blazed order). The diffracted waves are passed through another $4f$ system formed by lenses L3 ($f_3 = 75$ mm) and L4 ($f_4 = 400$ mm). The magnification of this $4f$ system is $M_2 = -f_4/f_3$. The lens L3 performs the Fourier transform of the diffracted waves in the second Fourier plane (FP2). In plane FP2, a mask is placed, which consists of a pinhole (10 μm diameter) and a circular hole (6 mm diameter). The prior aperture, located in FP1, low-pass filters the beam such that the diffracted orders are spatially separated in FP2, i.e. only light from the zeroth order passes through the circular hole. The pinhole filters down the blazed order to a point source, so that it approaches a plane wave after passing through the lens L4 (placed at focal distance from the pinhole), and acts as the reference wave in our setup. On the other hand, the zeroth order passes through the circular hole, and acts as the signal wave. These signal and reference waves interfere at an angle at the camera plane resulting in an off-axis interferogram, which encodes the phase information corresponding to the topography of the sample. For recording the interferogram, we used an Andor Neo Scientific CMOS camera (2560 $\times$ 2160 pixels, 16 bit, 6.5 $\times$ 6.5 μm^2 pixel size). The large camera sensor size allows us to inspect up to 16.6 $\times$

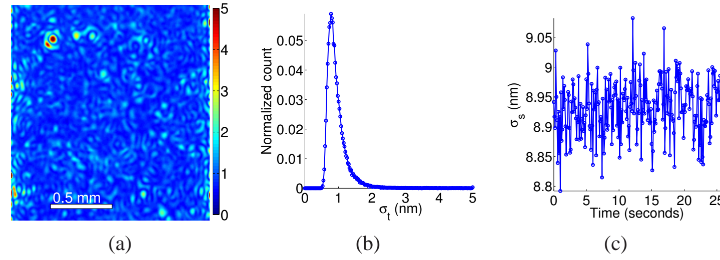

Fig. 2. (a) Temporal standard deviation $\sigma_t(x,y)$ of noise in nm. (b) Histogram of σ_t. (c) Spatial standard deviation $\sigma_s(t)$.

14 mm^2 area at the sample plane. Note that low pass-filtering at the two apertures in FP1 and FP2 limits the maximum sample spatial frequency to k_0NA_{min}, with $k_0 = 2\pi/\lambda$, and lowers the lateral resolution to $1.22\lambda/NA_{min}$, where NA_{min} is the numerical aperture corresponding to the smaller aperture. As the FP2 circular hole is the limiting aperture in our case, the instrument provides a resolution of about 87 μm for $NA_{min} = 0.0075$. To preserve transverse resolution, the size of the FP2 hole should be greater than or equal to that of the aperture in FP1. However, aliasing in the interferogram begins to occur when the beam diameter exceeds 8 mm [22]. Thus, we used a slightly smaller value (6 mm) to ensure there is no aliasing.

At the camera plane, denoting the signal wave as $U_s(x,y)$ and reference wave as $U_r(x,y) = U_1$, a constant, the recorded intensity can be expressed as,

$$I(x,y) = |U_s(x,y)|^2 + |U_1|^2 + 2|U_s(x,y)||U_1|\cos[\beta_0 x + \phi(x,y)] \tag{1}$$

which is essentially a cosinusoidal fringe pattern with spatial carrier frequency β_0 and phase distribution $\phi(x,y)$. Here, we have $\beta_0 = 2\pi/(|M_2|\Lambda)$, with Λ being the period of the grating. Note that the sampling frequency is $k_s = 2\pi/\Delta x$, with Δx being the pixel size, and the maximum spatial frequency of the interferogram given by Eq.(1), is $k_{max} = \beta_0 + k_0NA_{min}$. For our system, we have $k_s = 0.97$ radian/μm, $\beta_0 = 0.35$ radian/μm and $k_0NA_{min} = 0.09$ radian/μm. Hence, the Nyquist sampling criterion, i.e. $k_s \geq 2k_{max}$ is satisfied [22]. The phase $\phi(x,y)$ is related to the height distribution $h(x,y)$ of the sample as $h(x,y) = (\lambda/4\pi)\phi(x,y)$. For quantitative phase extraction, we apply the Hilbert transform [23] which provides the analytic signal associated with the real interferogram, and subsequently use Goldstein's phase unwrapping method [24].

The proposed setup exhibits several salient features: (1) both the reference and the signal waves traverse a common-path, which provides a compact system with increased robustness against misalignments and external disturbances, and high stability; (2) the net magnification of the system $M = M_1M_2 = 1$ i.e. unity, which implies that a large field of view can be analyzed; and (3) the diffraction grating introduces an angle between the reference and signal waves, resulting in an off-axis configuration, which permits phase retrieval from a single interferogram.

To characterize the temporal noise of the system, we used a Thorlabs mirror as the sample, and captured 256 time-lapsed interferograms (FOV 1.6 mm × 1.6 mm) at 10 frames/s. Subsequently, we recovered the height distribution from each interferogram. To analyze the temporal noise, the standard deviation with respect to time was computed for each pixel in the image. The resulting temporal standard deviation $\sigma_t(x,y)$ and its histogram are shown in Fig. 2(a) and Fig. 2(b). The median value of σ_t was obtained as 0.9 nm, which represents the temporal sensitivity, and indicates the high stability of the setup due to the common-path configuration. Similarly, we also computed the spatial standard deviation for each image; the resulting $\sigma_s(t)$ is shown in Fig. 2(c). The median value of σ_s was obtained as 8.9 nm, which represents the spatial sensitivity of our system.

#201422 - $15.00 USD Received 15 Nov 2013; revised 20 Dec 2013; accepted 14 Jan 2014; published 5 Feb 2014
(C) 2014 OSA

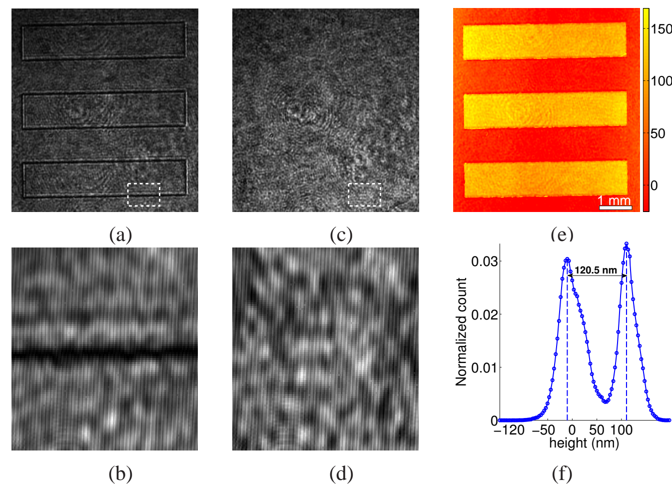

Fig. 3. Recorded interferograms for the (a) surface with features and (c) planar surface. For regions marked with white boxes in (a) and (c), the fringes are shown in (b) and (d). (e) Estimated height map in nm. (f) Histogram of height.

3. Results

To test the system's performance, we imaged a 1951 USAF resolution target (R3L3S1P) from Thorlabs. This standard target consists of a glass substrate on which the USAF features are deposited through chromium evaporation. These features exhibit a 120 nm step height difference with respect to the substrate. Further, to obtain uniform reflectivity, we coated the entire target with a gold/palladium layer of 25 $\pm$ 1 nm thickness using a Denton Vacuum sputter coater, while preserving the step height difference of the features. The interference image (FOV 5.9 mm $\times$ 5.7 mm) for the target is shown in Fig. 3(a). For an arbitrarily selected region (marked white) in Fig. 3(a), the fringes are clearly visible, as shown in Fig. 3(b). We also recorded the background interference image corresponding to a flat region of the target with no features, which is shown in Fig. 3(c), and the related marked region with visible fringes is shown in Fig. 3(d). Subtraction of the background phase from the sample phase removes any aberrations introduced by the system. Subsequently, the measured height map after background subtraction is shown in Fig. 3(e). Finally, we show the histogram of the height map in Fig. 3(f), which exhibits two dominant peaks, one corresponding to the background and the other corresponding to the features. From the histogram, the step height difference was obtained as 120.5 nm, which is extremely close to the predicted value. These results clearly show the high accuracy of the proposed technique for surface topography measurements involving large FOV samples.

Next, we demonstrate the utility of our technique for dynamic phase retardation measurement in a liquid crystal SLM. For our analysis, we used a liquid crystal on silicon (LCOS) based Holoeye Pluto phase-only reflective SLM as the sample. The projected pattern on the SLM at a given time instant is shown in Fig. 4(a). For dynamic behavior, the grayscale (GS) values of the central region of this pattern were linearly stepped from 0 (black) to 255 (white), with 1 level per time interval of 25 ms, whereas the outer region had a constant zero grayscale value. Using the high speed (40 frames/s) Andor Neo camera, we recorded several time-lapsed interferograms (FOV 3.3 mm $\times$ 3.3 mm), each corresponding to a particular pattern on the SLM. For the projected pattern in Fig. 4(a), the corresponding recorded interferogram is shown in Fig. 4(b). The temporally varying phase retardation can be expressed as,

$$\phi(x,y,t) = \frac{4\pi}{\lambda}\Delta n(x,y,t)d \tag{2}$$

#201422 - $15.00 USD Received 15 Nov 2013; revised 20 Dec 2013; accepted 14 Jan 2014; published 5 Feb 2014
(C) 2014 OSA

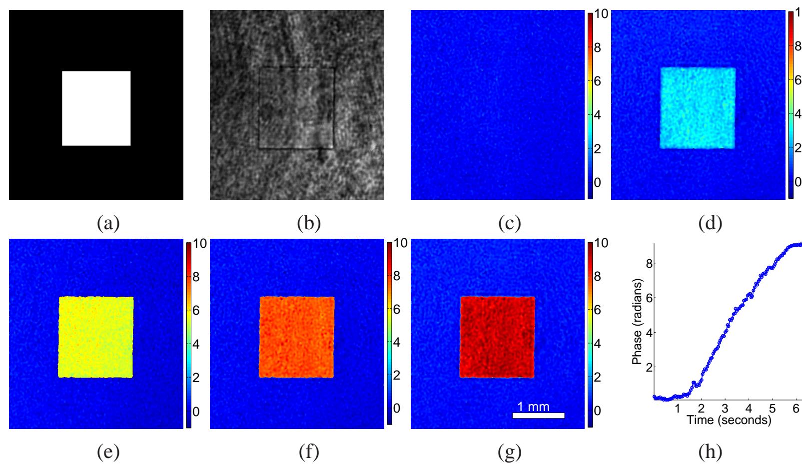

Fig. 4. (a) Projected pattern on SLM. (b) Recorded interferogram. Measured phase retardation in radians at (c) $t = 0$, GS=0, (d) $t = 2.5$, GS=100, (e) $t = 3.75$, GS=150, (f) $t = 5$, GS=200, and (g) $t = 6.25$ seconds, GS=250 (see Media 1). (h) Temporally varying mean phase retardation.

where $\Delta n = n_e - n_o$ is the birefringence, with n_e and n_o being the refractive indices along the extraordinary and ordinary axis, and d is the thickness of the liquid crystal in SLM.

For phase extraction, the dynamic case presents an interesting challenge. The phase corresponding to the central region keeps increasing with time, whereas it remains constant for the outer region. As a result, for a given time instant, the phase difference between adjacent pixels corresponding to the central region and the outer region can easily exceed π, which is the phase aliasing limit [24]. Thus, any spatial phase unwrapping algorithm such as the Goldstein's method would provide erroneous results. To circumvent this problem, we performed the unwrapping operation along the temporal direction [25], which avoids phase aliasing. The computed phase retardation values from the interferograms at different time instants are shown in Figs. 4(c)-4(g). Note that we also recorded a background image corresponding to the zero grayscale projected pattern, and performed background subtraction to ensure that the measured phase has no contributions arising from the SLM height variations or system aberrations. The temporally varying phase retardation is also shown in Media 1. Finally, the mean phase retardation, computed along the temporally varying central region is shown in Fig. 4(h). These results clearly demonstrate the suitability of the proposed technique for dynamic measurements. Also, due to the inherent stability of the instrument, we can dynamically measure the phase shifts vs grayscale values across the entire spatial light modular area. Consequently, this approach provides a new way of real-time spatial light modulator calibration.

4. Conclusions

We introduced a quantitative phase imaging technique for wide-field metrology. Compared to the existing methods, it offers the ability to analyze large field of view objects with nanometric accuracy and exhibits high temporal stability for performing high precision measurements, both static and dynamic. In addition, the technique's advantages include non-invasive nature, single-shot methodology and full-field measurement capability. It has significant application potential in non-destructive metrology and characterization of liquid crystal modulators.

#201422 - $15.00 USD Received 15 Nov 2013; revised 20 Dec 2013; accepted 14 Jan 2014; published 5 Feb 2014
(C) 2014 OSA

Acknowledgments

This research was supported in part by the National Science Foundation (grant CBET-1040462 MRI). Gannavarpu Rajshekhar is supported by the Swiss National Science Foundation fellowship. We thank Scott Robinson for assistance with sputter coating.